LETTERS
PUBLISHED ONLINE: 8 DECEMBER 2013 | DOI: 10.1038/NMAT3826
nature materials

Crossover from incoherent to coherent phonon scattering in epitaxial oxide superlattices

Jayakanth Ravichandran[1,2†‡], Ajay K. Yadav[2,3‡], Ramez Cheaito[4‡], Pim B. Rossen[3], Arsen Soukiassian[5], S. J. Suresha[2], John C. Duda[4], Brian M. Foley[4], Che-Hui Lee[5], Ye Zhu[6], Arthur W. Lichtenberger[7], Joel E. Moore[2,8], David A. Muller[6,9], Darrell G. Schlom[5,9], Patrick E. Hopkins[4], Arun Majumdar[10], Ramamoorthy Ramesh[1,2,3,8,11★] and Mark A. Zurbuchen[12,13,14★]

Elementary particles such as electrons[1,2] or photons[3,4] are frequent subjects of wave-nature-driven investigations, unlike collective excitations such as phonons. The demonstration of wave–particle crossover, in terms of macroscopic properties, is crucial to the understanding and application of the wave behaviour of matter. We present an unambiguous demonstration of the theoretically predicted crossover from diffuse (particle-like) to specular (wave-like) phonon scattering in epitaxial oxide superlattices, manifested by a minimum in lattice thermal conductivity as a function of interface density. We do so by synthesizing superlattices of electrically insulating perovskite oxides and systematically varying the interface density, with unit-cell precision, using two different epitaxial-growth techniques. These observations open up opportunities for studies on the wave nature of phonons, particularly phonon interference effects, using oxide superlattices as model systems, with extensive applications in thermoelectrics and thermal management.

Macroscopic coherent transport of particles in materials takes advantage of their wave rather than their particle nature. Such phenomena are the consequence of the quantum-mechanical nature of particles such as electrons, photons and phonons. Despite widespread and versatile demonstrations of coherent wave transport of electrons[1,2] and photons[3,4], demonstrations of coherent wave transport of phonons have been limited to spectroscopic experiments[5,6]. Typical experiments on the wave nature of phonons have focused on the generation and detection of short-lived, largely monochromatic optical and acoustic phonons using laser pump–probe techniques[5] and superconducting tunnel junctions[6], or, alternatively, the ballistic wave nature of phonons at length scales comparable to their wavelength[7–9]. Despite these advancements in accessing coherent phonons using spectroscopic techniques, owing to the short coherence length of phonons, demonstration of wave effects on macroscopic thermal transport quantities has been elusive so far. The presence of defects, interfaces, surface imperfections, anharmonicity and mode conversions can lead to decoherence of phonons, making the unambiguous observation of wave behaviour extremely challenging.

Superlattices[10,11] are the ideal model systems for the realization and understanding of coherent phonon effects on macroscopic thermal properties, particularly the wave–particle crossover. Thermal transport in superlattices has been the subject of several experimental[10–17] and theoretical investigations[18–23]. One of the important and long-standing predictions regarding thermal transport across superlattices (that is, along the layering axis) is the existence of a minimum in thermal conductivity as a function of the interface density, an indication of the crossover from particle-like to wave-like transport of phonons[18]. So far, conventional semiconductors such as silicon/germanium or GaAs/AlAs have been employed as model systems in pursuit of the experimental observation of the thermal conductivity minimum, owing to decades of perfecting their growth by molecular-beam epitaxy (MBE). These efforts have been largely fruitless owing to the presence of electronic charge carriers[11,14] and/or imperfect interfaces or defects such as dislocations[12,13,16,17]. The most promising system, GaAs/AlAs, has not shown a clear minimum in thermal conductivity as a function of interface density that would highlight the wave–particle crossover[24].

There are a couple of materials parameters, which can guide us in selecting an ideal superlattice for the thermal conductivity minimum. The maximum in bulk thermal conductivity as a function of temperature signifies the temperature at which the Umklapp scattering becomes dominant and occurs at ~100 K for $SrTiO_3$ (ref. 25) and ~30–50 K for silicon[26] and GaAs (ref. 27). Another parameter that could be relevant is the phonon coherence length[23]. The calculated coherence length for longitudinal and transverse modes is ~2 nm and 1 nm for GaAs (ref. 23) and ~4.5 and 3 nm for $SrTiO_3$, respectively (more information on the calculations is available in the Supplementary Information). Thus, the longer phonon coherence length and favourable Umklapp peak suggest that perovskite

[1]Applied Science and Technology Graduate Group, University of California, Berkeley, California 94720, USA, [2]Materials Sciences Division, Lawrence Berkeley National Laboratory, Berkeley, California 94720, USA, [3]Department of Materials Science and Engineering, University of California, Berkeley, California 94720, USA, [4]Department of Mechanical and Aerospace Engineering, University of Virginia, Charlottesville, Virginia 22904, USA, [5]Department of Materials Science and Engineering, Cornell University, Ithaca, New York 14853, USA, [6]School of Applied and Engineering Physics, Cornell University, Ithaca, New York 14853, USA, [7]Department of Electrical and Computer Engineering, University of Virginia, Charlottesville, Virginia 22904, USA, [8]Department of Physics, University of California, Berkeley, California 94720, USA, [9]Kavli Institute at Cornell for Nanoscale Science, Cornell University, Ithaca, New York 14853, USA, [10]ARPA-E, US Department of Energy, 1000 Independence Avenue, Washington DC 20585, USA, [11]Oak Ridge National Laboratory, Oak Ridge, Tennessee 37831, USA, [12]Department of Materials Science and Engineering, University of California, Los Angeles, California 90095, USA, [13]Western Institute of Nanoelectronics, Department of Electrical Engineering, University of California, Los Angeles, California 90095, USA, [14]California NanoSystems Institute, University of California, Los Angeles, California 90095, USA. †Present address: Department of Physics, Columbia University, New York, New York 10027, USA. ‡These authors contributed equally to this work. *e-mail: rramesh@berkeley.edu; mark_z@mac.com

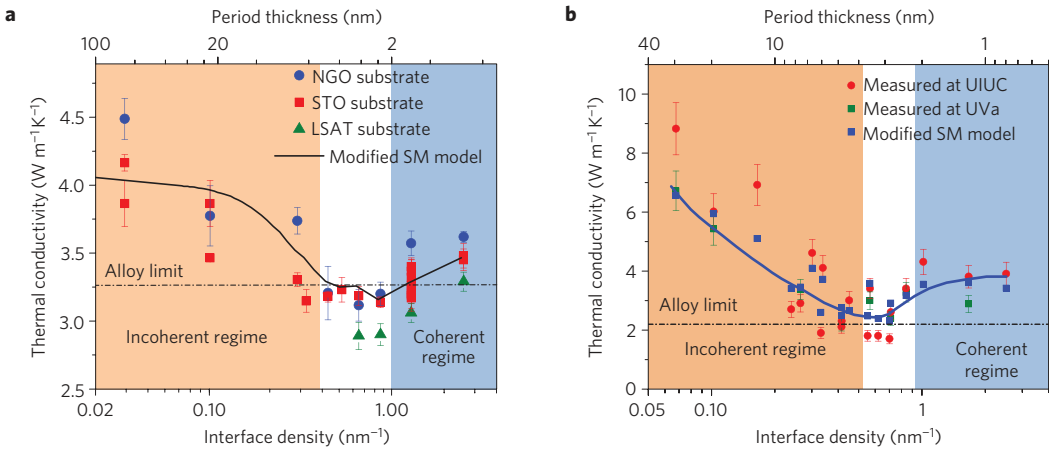

Figure 1 | Measured thermal conductivity values for superlattices as a function of interface density at room temperature. a, $(STO)_m/(CTO)_n$ superlattice. **b**, $(STO)_m/(BTO)_n$ superlattice. The black line represents the modified Simkin–Mahan (SM) model with disorder correction for $(STO)_m/(CTO)_n$ superlattices and the blue dots represent the Simkin–Mahan model with disorder and volume fraction corrections for $(STO)_m/(BTO)_n$ superlattices. The blue line is used as a guide to eye. The black dot–dash horizontal lines refer to the experimentally measured thermal conductivity for STO/CTO 50:50 alloy and the STO/BTO 25:75 alloy and are designated as the alloy limits. Error bars in the figures represent the error due to standard deviation and uncertainties in the measurement. Detailed error analysis is available in the Supplementary Information.

oxides could be a suitable materials system to explore the thermal conductivity minimum. This coupled with the availability of a rich variety of chemically and structurally compatible perovskites with different acoustic impedance mismatches, tunable through chemical substitutions, makes perovskites an attractive system. Furthermore, the availability of perovskite substrates spanning the range of lattice parameters of interest[28] and atomically abrupt perovskite oxide surfaces with controlled growth processes such as laser MBE (ref. 29) and MBE (ref. 30), in conjunction with precise surface treatment procedures[31], has made high-quality oxide superlattices with atomically sharp interfaces[32] realizable.

Here, we report the physical demonstration of the phonon scattering crossover in high-quality perovskite superlattices of $SrTiO_3/CaTiO_3$ and $SrTiO_3/BaTiO_3$ with atomically sharp interfaces. Our results provide indirect evidence for the formation of phonon mini-bands and hence, phonon interference effects in these superlattices[18]. We grew the epitaxial superlattices coherently on various single-crystal oxide substrates using two different growth techniques, yielding superlattices with minimal disorder, thus confirming the generic and robust nature of this effect in electrically insulating superlattices. Our simple theoretical model also highlights the necessity to minimize corrections due to differences in volume fraction of the species and interface disorder, to observe a clear minimum in thermal conductivity as a function of interface density. We also show that these superlattices beat the alloy limit by interface scattering alone.

Epitaxial superlattices of $(SrTiO_3)_m/(CaTiO_3)_n$ (notation: $(STO)_m/(CTO)_n$) and $(SrTiO_3)_m/(BaTiO_3)_n$ (notation: $(STO)_m/(BTO)_n$), where m and n refer to the thickness, in unit cells, of the $(001)_{pc}$-oriented (pseudo-cubic) perovskite layers, respectively, were grown using reflection high-energy electron diffraction (RHEED)-assisted laser MBE and conventional MBE techniques. In the case of $(STO)_m/(CTO)_n$ superlattices, the thickness of each layer in a period was adjusted to vary the interface density, but keeping the volume fraction of the constituents and total thickness of the films constant (the thickness was set at 200 nm and the rationale behind choosing this number is explained in terms of thermal penetration depth calculations in the Supplementary Information) to eliminate any role of size effects[9]. The volume fractions of STO and CTO were maintained at 50:50, and the superlattice period thicknesses were varied to span interface densities from 0.025 to 2.59 nm^{-1}. By keeping these variables constant and varying only the interface density, these synthesis experiments provide the best platform to unambiguously observe coherent phonon phenomena in superlattices. $(STO)_m/(CTO)_n$ superlattices were also grown by MBE on (001) LSAT substrates. The $(STO)_m/(BTO)_n$ superlattices were grown on $(001)_{pc}$-oriented single-crystal STO and $TbScO_3$ substrates by conventional MBE from elemental sources. The thicknesses of these superlattices were varied from 57 to 293 nm, and the interface densities varied from 0.068 to 2.51 nm^{-1} with varying volume fractions of STO and BTO. Thermal conductivity in the cross-plane direction of the superlattices was measured by time-domain thermoreflectance (TDTR) for both the superlattice systems[33]. (A detailed account of the parameters related to sample preparation, measurement and analysis in this study is provided in the Supplementary Information.)

The primary result of the work is summarized in Fig. 1. The plots in Fig. 1a,b show the thermal conductivity at room temperature measured on $(STO)_m/(CTO)_n$ and $(STO)_m/(BTO)_n$ superlattices, respectively, as a function of the interface density, measured alloy thermal conductivity values for STO/CTO 50:50 and STO/BTO 25:75 alloys and the theoretically calculated thermal conductivity values based on a simple Simkin–Mahan model[18] (details explained in Supplementary Information). In both cases, the plot can be clearly divided into two regimes based on whether the thermal conductivity increases (coherent) or decreases (incoherent) with increasing interface density. In the low interface-density regime, the system can be modelled as a series of bulk thermal resistances with the resistance of the interfaces added in series with the bulk resistances. In this incoherent regime, the behaviour of the phonons is particle-like and hence the thermal resistance increases linearly with increasing interface density. At the high interface-density regime, where the superlattice period is comparable to the coherence length of the phonons, the wave nature of phonons must be considered. In this limit, the superlattice phonon dispersion forms mini-bands owing to band folding along the cross-plane axis, which decreases the overall group velocity of the high-frequency phonon modes. As the interface density increases, the number of mini-bands decreases and this leads to an increase in average phonon group velocity. Thus, the observation of a minimum in thermal conductivity as a function of interface density is direct evidence of the crossover from incoherent to coherent phonon transport in these superlattices. We clearly observe this minimum even in the room-temperature measurements presented in Fig. 1.

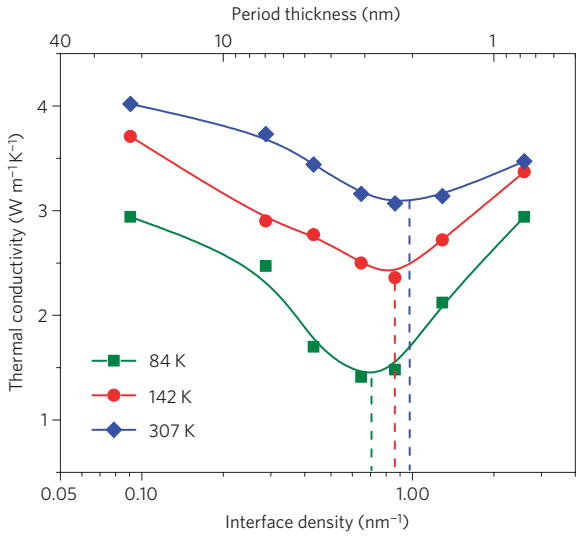

Figure 2 | Measured thermal conductivity values for $(STO)_m/(CTO)_n$ superlattices as a function of interface density at different temperatures. The minimum in thermal conductivity becomes deeper at lower temperatures and the interface density at which the minimum occurs moves to smaller values at lower temperatures as expected. The solid lines are guides to the eye. The shift of the minimum is shown using dashed lines projected onto the *x* axis for different temperatures.

We note that equivalent (STO)/(CTO) superlattice films on NGO ($NdGaO_3$) substrates tend to have slightly higher thermal conductivity than those on STO or LSAT substrates. All are of identical thickness, so this cannot be attributed to the thickness-dependent effect noted previously[7]. The observation also cannot be attributed to the differing symmetry of the orthorhombic NGO versus the cubic symmetry of STO and LSAT. NGO is a slightly distorted perovskite, and a NGO (110) surface presents a square surface mesh to within 0.3% by bond distance, and within 0.002% by symmetry. Therefore, symmetry or octahedral distortion differences due to different substrates can be ruled out as a dominant contributing factor (although such distortions of CTO or BTO may occur in the superlattices themselves, especially the longer-period ones). The difference in the lattice parameter of NGO (110) and LSAT (001) surfaces as compared with STO (001) is −1.1% (average of −0.9 and −1.3%) and −0.9%, respectively, and so strain could play a subtle and systematic role in varying the thermal conductivity of superlattices grown on different substrates. We have seen minor hints of a possible misfit effect on thermal conductivity, and this is the subject of ongoing efforts. The origin of this systematic difference in thermal conductivity between superlattices on different substrates could be due to a combination of the above-discussed effects. Last, we note that, although only short-period (STO)/(CTO) superlattices on LSAT substrates were synthesized and measured, these data are taken in the important (coherent) regime. The incoherent regime is known to exhibit a classical trend of thermal conductivity with decreasing interface density, trending in the limit towards a thermal conductivity that is an average of the two components, STO and CTO.

Figure 2 shows the thermal conductivity of $(STO)_m/(CTO)_n$ superlattices at 307, 142 and 84 K for a range of interface densities. There are two clear trends observable in this plot. First, the depth of the minimum increases with decreasing temperature, and second, the interface density at the minimum shifts to lower values at lower temperatures. Both of these trends are consistent with the zone-folded mini-band formation description[18,19]. The temperature window in which the minimum can be observed is limited. If the temperature is too high, Umklapp processes will dominate and limit the observation of such coherent behaviour; at too low temperatures the high-frequency phonon modes may not be populated or may carry insufficient heat to show a very pronounced minimum. The observation of a minimum over a temperature range with a clear trend further corroborates our conclusion of the observation of coherent wave scattering phenomena at high interface densities in these superlattices.

Structural and microstructural characterizations of superlattice samples are shown in Fig. 3. The results establish the crystalline perfection of the bulk, interfaces, and layering of the superlattices. Figure 3a shows a high-resolution, short-angular-range θ–2θ X-ray diffraction (XRD) scan of a $(STO)_6/(CTO)_6$ superlattice centred on the substrate 220 peak. The data clearly show the 002 Bragg peak roughly corresponding to a 50:50 STO/CTO alloy with a single order of superlattice fringes, labelled $SL_{(\pm1)}$. Figure 3b similarly shows a θ–2θ XRD scan, in this case of a $(STO)_{74}/(BTO)_1$ superlattice, collected over a 2θ angular range of 40°–52.5°. The plot shows a strong peak from the substrate, and many orders of superlattice reflections, indicating the high degree of long-range order of the superlattice itself. Evaluating the strain relaxation and the rocking curves of the films also aids in assessing the low occurrence of line defects such as misfit dislocations. Qualitative evidence for this high degree of crystalline perfection is shown in Fig. 3c, in terms of a reciprocal space map of the $(STO)_2/(CTO)_2$ superlattice. The map clearly shows that the in-plane lattice parameter of the film matches well with the substrate (similar reciprocal-space maps for superlattices about the minimum are given in the Supplementary Information) and hence is coherently strained with the substrate. As there is little or no strain relaxation, we can rule out the formation of a significant density of misfit dislocations, which would have affected thermal transport. Moreover, the full-width at half-maximum (FWHM) values for the rocking curves of the $(STO)_6/(CTO)_6$ superlattice 002 peaks and substrate 002 peaks were 0.028° and 0.018°, respectively. Similarly, the FWHM for the rocking curves of the substrates and $(STO)_m/(BTO)_n$ superlattices averaged 0.018° and 0.023°, respectively, with film texture commensurate with substrate in each case. A narrow FWHM (typically limited by the broadening due to crystalline domains and threading dislocations from the substrate) for a film, which is comparable to the substrate, is a further indication of the lack of misfit dislocations and other line defects.

The presence of thickness fringes (Pendellösung fringes) surrounding the central Bragg peak in Fig. 3a attests to the surface smoothness of the film. The smoothness of the surface of the $(STO)_m/(CTO)_n$ superlattices was evaluated by atomic force microscopy, as shown in Fig. 3d, revealing that the film surface remains smooth with unit-cell terraces even after growing a 200-nm-thick film (further discussions can be found in the Supplementary Information). Results of transmission electron microscopy (TEM) characterization of both films are shown in Fig. 3e,f for $(STO)_m/(CTO)_n$ and $(STO)_m/(BTO)_n$ superlattices, respectively. Figure 3e shows cross-sectional scanning TEM (STEM) analysis of a $(STO)_2/(CTO)_2$ superlattice. The image clearly shows that the interfaces obtained by the laser MBE growth technique are extremely sharp with little or no inter-diffusion of species across the interfaces. Figure 3f shows a cross-sectional STEM electron energy loss spectroscopy (STEM-EELS) map of the Ti and Ba atoms in a $(STO)_{30}/(BTO)_1$ superlattice using Ti–$L_{2,3}$ edges (green) and Ba–$M_{4,5}$ edges (purple), along with a schematic of the crystal structure. This documents the atomically sharp interfaces that are created in the oxide superlattices by MBE. In summary, these characterizations clearly establish the high quality of the superlattice samples. (Further structural analysis on both the $(STO)_m/(CTO)_n$ and $(STO)_m/(BTO)_n$ superlattices can be found in the Supplementary Information.)

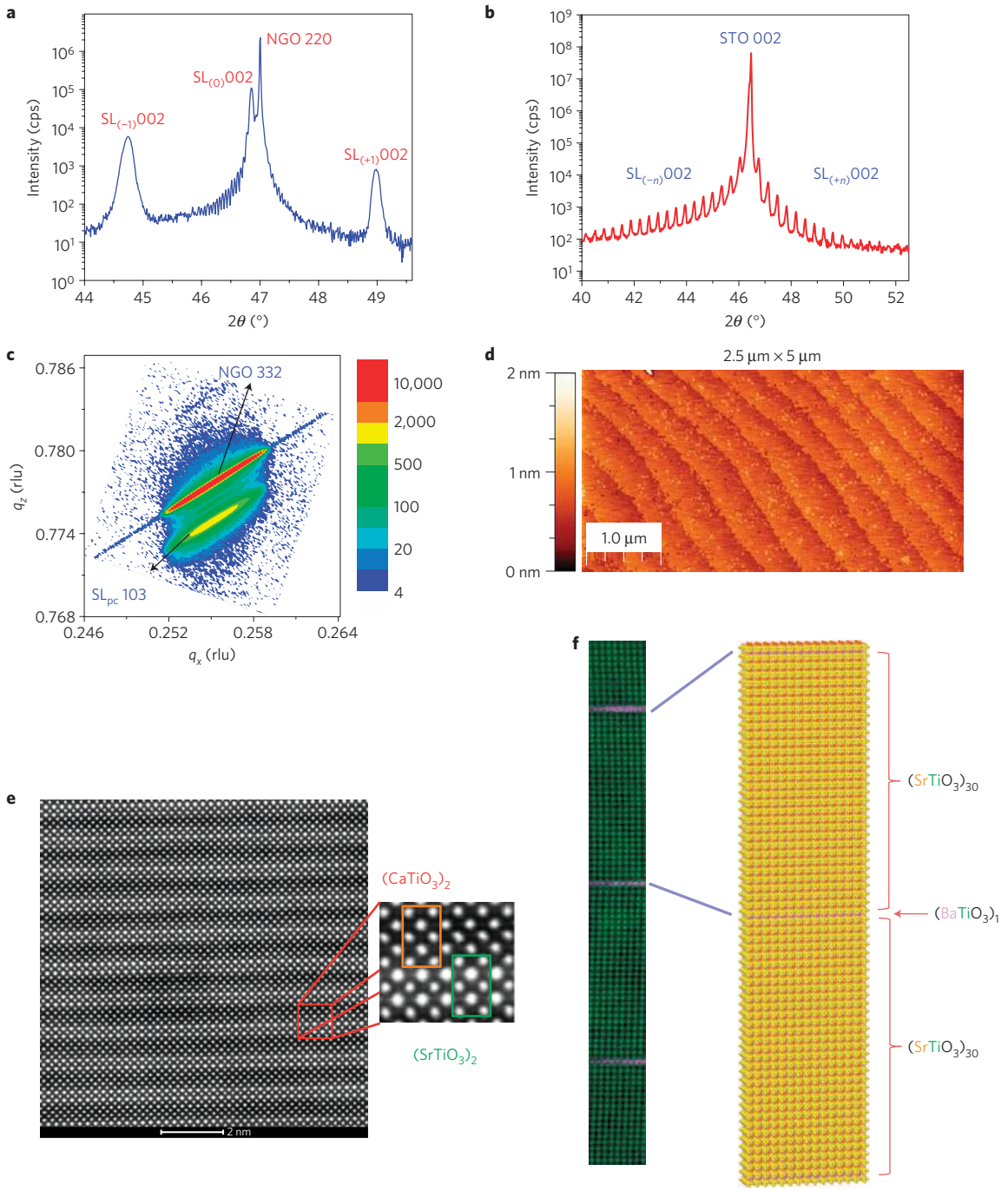

Figure 3 | Structural and microstructural characterization of superlattice samples from both series. a,**b**, High-resolution, short angular-range θ–2θ XRD scan of a $(STO)_6/(CTO)_6$ superlattice centred on the NGO 220 substrate peak (**a**) and $(STO)_{74}/(BTO)_1$ superlattice peaks centred on the STO 002 substrate peak (**b**). Both the superlattice peaks and the thickness fringes suggest the high degree of interface abruptness in the samples. **c**, A high-resolution reciprocal space map of the $(STO)_2/(CTO)_2$ superlattice centred on the NGO 332 substrate peak. The map clearly shows that the superlattice film is coherently strained to the substrate. The colour scale bar indicates intensity in arbitrary units (log scale). **d**, Surface topography of a 200 nm $(STO)_2/(CTO)_2$ thick superlattice film on a STO (001) substrate. The image clearly shows the presence of smooth step edges with unit-cell height. **e**,**f**, High-angle annular dark-field (HAADF) STEM images of $(STO)_2/(CTO)_2$ (**e**) and STEM-EELS image (dimensions 35 nm × 3.6 nm) of a $(STO)_{30}/(BTO)_1$ superlattice (**f**) revealing the presence of atomically sharp interfaces with minimal intermixing in the samples studied. A schematic of the crystal structures is shown on the right in **f**. Chemical formulae of the component materials of the superlattice are colour-coded to match the false-colour of the atomic-resolution STEM-EELS image on the left (Sr, orange; Ba, purple; Ti, green).

In conclusion, we have provided the first unambiguous evidence for the crossover of phonon scattering from particle-like (incoherent) to wave-like (coherent) processes in high-quality, epitaxial perovskite oxide superlattices. The results are in agreement with several theoretical predictions, and are much stronger evidence for coherent phonon transport than the often-reported ballistic transport experiments[7–9]. We have also shown sufficient evidence to eliminate extraneous or spurious effects, which could have alternatively explained the observed thermal conductivity minimum in these superlattices. Our work opens up

several opportunities, where we can harness this wave nature to demonstrate thermal transport processes, which are not possible in a normal diffusive framework. Complete destructive interference of these phonons can lead to phonon localization and hence to very low thermal conductivities in crystalline systems. Low thermal conductivities in macroscopic crystalline systems, by taking advantage of the wave behaviour of phonons, are anticipated to enable advances in new heat transfer applications. Last, these perovskite superlattice-based heterostructures can also function as a basic building block for experiments targeting phonon optics.

Received 5 June 2013; accepted 30 October 2013; published online 8 December 2013

References

1. Venema, L. C. *et al.* Imaging electron wave functions of quantized energy levels in carbon nanotubes. *Science* **283,** 52–55 (1999).
2. Liang, W. *et al.* Fabry–Perot interference in a nanotube electron waveguide. *Nature* **411,** 665–669 (2001).
3. Heavens, O. S. & Ditchburn, R. W. *Insight Into Optics* (Wiley, 1992).
4. Born, M. & Wolf, E. *Principles of Optics* (CUP, 1999).
5. Trigo, M., Bruchhausen, A., Fainstein, A., Jusserand, B. & Thierry-Mieg, V. Confinement of acoustical vibrations in a semiconductor planar phonon cavity. *Phys. Rev. Lett.* **89,** 227402 (2002).
6. Narayanamurti, V., Stormer, H. L., Chin, M. A., Gossard, A. C. & Wiegmann, W. Selective transmission of high-frequency phonons by a superlattice: The 'dielectric' phonon filter. *Phys. Rev. Lett.* **43,** 2012–2016 (1979).
7. Luckyanova, M. N. *et al.* Coherent phonon heat conduction in superlattices. *Science* **338,** 936–939 (2012).
8. Siemens, M. E. *et al.* Quasi-ballistic thermal transport from nanoscale interfaces observed using ultrafast coherent soft X-ray beams. *Nature Mater.* **8,** 1–5 (2009).
9. Cheaito, R. *et al.* Experimental investigation of size effects on the thermal conductivity of silicon–germanium alloy thin films. *Phys. Rev. Lett.* **109,** 195901 (2012).
10. Capinski, W. S. & Maris, H. J. Thermal conductivity of GaAs/AlAs superlattices. *Physica B* **219–220,** 699–701 (1996).
11. Venkatasubramanian, R. Lattice thermal conductivity reduction and phonon localization-like behavior in superlattice structures. *Phys. Rev. B* **61,** 3091–3097 (2000).
12. Lee, S. M., Cahill, D. G. & Venkatasubramanian, R. Thermal conductivity of Si–Ge superlattices. *Appl. Phys. Lett.* **70,** 2957–2959 (1997).
13. Touzelbaev, M. N., Zhou, P., Venkatasubramanian, R. & Goodson, K. E. Thermal characterization of Bi_2Te_3/Sb_2Te_3 superlattices. *J. Appl. Phys.* **90,** 763–766.
14. Rawat, V., Koh, Y. & Cahill, D. Thermal conductivity of (Zr,W)N/ScN metal/semiconductor multilayers and superlattices. *J. Appl. Phys.* **105,** 024909 (2009).
15. Koh, Y. K., Cao, Y., Cahill, D. G. & Jena, D. Heat-transport mechanisms in superlattices. *Adv. Funct. Mater.* **19,** 610–615 (2009).
16. Chakraborty, S. *et al.* Thermal conductivity in strain symmetrized Si/Ge superlattices on Si(111). *Appl. Phys. Lett.* **83,** 4184–4186 (2003).
17. Huxtable, S. T. *et al.* Thermal conductivity of Si/SiGe and SiGe/SiGe superlattices. *Appl. Phys. Lett.* **80,** 1737–1739 (2002).
18. Simkin, M. & Mahan, G. Minimum thermal conductivity of superlattices. *Phys. Rev. Lett.* **84,** 927–930 (2000).
19. Chen, Y., Li, D., Lukes, J. & Ni, Z. Minimum superlattice thermal conductivity from molecular dynamics. *Phys. Rev. B* **72,** 174302 (2005).
20. Termentzidis, K., Chantrenne, P., Duquesne, J-Y. & Saci, A. Thermal conductivity of GaAs/AlAs superlattices and the puzzle of interfaces. *J. Phys. Condens. Matter* **22,** 475001 (2010).
21. Garg, J., Bonini, N. & Marzari, N. High thermal conductivity in short-period superlattices. *Nano Lett.* **11,** 5135–5141 (2011).
22. Chernatynskiy, A., Grimes, R. W., Zurbuchen, M. A., Clarke, D. R. & Phillpot, S. R. Crossover in thermal transport properties of natural, perovskite-structured superlattices. *Appl. Phys. Lett.* **95,** 161906 (2009).
23. Chen, G. Size and interface effects on thermal conductivity of superlattices and periodic thin-film structures. *J. Heat Transf.* **119,** 220–229 (1997).
24. Capinski, W. S. *et al.* Thermal-conductivity measurements of GaAs/AlAs superlattices using a picosecond optical pump-and-probe technique. *Phys. Rev. B* **59,** 8105–8113 (1999).
25. Oh, D-W. *et al.* Thermal conductivity as a metric for the crystalline quality of $SrTiO_3$ epitaxial layers. *Appl. Phys. Lett.* **98,** 221904 (2011).
26. Glassbrenner, C. & Slack, G. Thermal conductivity of silicon and germanium from 3° K to the melting point. *Phys. Rev.* **134,** A1058–A1069 (1964).
27. Carlson, R. O., Slack, G. A. & Silverman, S. J. Thermal conductivity of GaAs and $GaAs_{1-x}P_x$ laser semiconductors. *J. Appl. Phys.* **36,** 505–507 (1965).
28. Uecker, R. *et al.* Properties of rare-earth scandate single crystals (Re = Nd–Dy). *J. Cryst. Growth* **310,** 2649–2658 (2008).
29. Ohtomo, A., Muller, D. A., Grazul, J. L. & Hwang, H. Y. Artificial charge-modulation in atomic-scale perovskite titanate superlattices. *Nature* **419,** 378–380 (2002).
30. Jiang, J. C., Pan, X. Q., Tian, W., Theis, C. D. & Schlom, D. G. Abrupt $PbTiO_3/SrTiO_3$ superlattices grown by reactive molecular beam epitaxy. *Appl. Phys. Lett.* **74,** 2851–2853 (1999).
31. Kawasaki, M. *et al.* Atomic control of the $SrTiO_3$ crystal surface. *Science* **266,** 1540–1542 (1994).
32. Schlom, D. G., Chen, L. Q., Pan, X., Schmehl, A. & Zurbuchen, M. A. A thin film approach to engineering functionality into oxides. *J. Am. Ceram. Soc.* **91,** 2429–2454 (2008).
33. Cahill, D. G. Analysis of heat flow in layered structures for time-domain thermoreflectance. *Rev. Sci. Instrum.* **75,** 5119–5122 (2004).

Acknowledgements

The work on $SrTiO_3/CaTiO_3$ superlattices was supported by the US Department of Energy, Office of Basic Energy Sciences under Contract No. DE-AC02-05CH11231. The work on $SrTiO_3/BaTiO_3$ superlattices by A.S., C-H.L., D.G.S. and M.A.Z. was supported by the Defense Advanced Research Projects Agency (DARPA) and the US Army Aviation and Missile Research, Development, and Engineering Center (AMRDEC) through Grant No. W31P4Q-09-1-0005. TEM sample preparation for some of the $SrTiO_3/BaTiO_3$ superlattices was performed by the UCLA Nanoelectronics Research Facility. We acknowledge the use of instruments at the Electron Imaging Center for NanoMachines (EICN) supported by NIH (1S10RR23057 to Z.H.Z.) at the California NanoSystems Institute (CNSI), UCLA. Electron microscopy and spectroscopy of $SrTiO_3/BaTiO_3$ at Cornell by Y.Z. and D.A.M. was supported by the Army Research Office (ARO) grant W911NF-09-1-0415 and the electron microscopy facility of the Cornell Center for Materials Research (CCMR) by the National Science Foundation Materials Research Science and Engineering Centers (MRSEC) programme (DMR 1120296). P.E.H. is grateful for financial support from Army Research office (ARO) grant W911NF-13-1-0378. TDTR measurements on the $SrTiO_3/CaTiO_3$ superlattices at the University of Virginia were supported by the National Science Foundation (NSF) grant CBET-1339436. J.R. acknowledges the fellowship from Link Foundation. The authors wish to express deep gratitude to D. G. Cahill for measuring the thermal conductivity of a significant number of the samples by TDTR, and for many thoughtful discussions. The authors also wish to acknowledge the contributions of CrysTec GmbH for providing the high-quality single-crystal substrates that were used in this study.

Author contributions

J.R. and P.E.H. designed the experiments on STO/CTO superlattices and M.A.Z. designed the experiments on STO/BTO superlattices. A.K.Y., P.B.R., J.R. and A.S. grew and characterized the samples for STO/CTO superlattice work, and A.S. and C-H.L. grew the samples for STO/BTO superlattice work. R.C., J.C.D., B.M.F. and P.E.H. measured and analysed the thermal conductivity of samples. S.J.S., M.A.Z., Y.Z. and D.A.M. performed TEM studies. A.W.L. assisted in TDTR experiments at UVa. J.E.M. performed the Simkin–Mahan model calculations and J.R. carried out the coherence length calculations and scaling analysis to modify the Simkin–Mahan model. J.R., P.E.H., M.A.Z., A.K.Y. and R.C. co-wrote the manuscript. R.R., A.M., D.G.S. and M.A.Z. supervised the research. All authors contributed to the discussions and manuscript preparation.

Additional information

Supplementary information is available in the online version of the paper. Reprints and permissions information is available online at www.nature.com/reprints. Correspondence and requests for materials should be addressed to R.R. or M.A.Z.

Competing financial interests

The authors declare no competing financial interests.